Supplement of

Influence of heterogeneous thermal conductivity on the long-term evolution of the lower-mantle thermochemical structure: implications for primordial reservoirs

Joshua Martin Guerrero et al.

Correspondence to: Joshua Martin Guerrero (joshua@earth.sinica.edu.tw) and Frédéric Deschamps (frederic@earth.sinica.edu.tw)

Content of the supplement

5

10

S1 Introduction

Supplement contains Sect. S2 and S3, which outlines the details of the numerical model and its main characteristics, details regarding converting between potential temperature and full (including the adiabat) temperature, definitions of mantle structures including plume and downwelling regions, and the calculation of derived physical parameters including the average height and the density anomaly profiles associated with thermochemical material, Table S1, listing all parameters and dimensional scale for our simulations, Table S2, listing simulation averages centred at $t = 9.0$ Gyr, Table S3, listing simulation averages between $t = 3$ and 11.2 Gyr, Table S4, listing simulation averages for case no. 17 with different initial conditions, and Figures S1 to S17.

S2 Details of numerical simulations

We model compressible thermochemical mantle convection using the finite-volume code StagYY. The conservation equations of mass, energy, momentum, and composition are solved on a 2D spherical annulus domain (e.g., Hernlund & Tackley, 2008). Details of the numerical techniques used to solve this system may be found in Tackley (2008). All simulations are computed non-dimensionally and can be dimensionalized using input and scaling parameters listed in Table S1. Dimensionalizing temperature requires correcting for adiabatic compression effects and is detailed in Sect. S3. The main properties of our model are discussed below.

S2.1 Geometry and general physical properties

Each calculation is performed in a 2D spherical annulus domain, which emulates convection in a variable-thickness slice of a spherical shell centred at the Equator. The spherical annulus is characterized with a curvature factor $f = 0.55$ (calculated from the ratio of core-mantle boundary radius to surface radius) and the domain is subdivided into a radial resolution and lateral resolution of 128 and 2048 grid points, respectively. Additional grid refinement is specified at the surface and core-mantle boundaries as well as the 660-km transition to ensure that the flow is well resolved in those regions. The annulus domain features a wrapping side boundaries and free-slip surface and core-mantle boundaries. The surface temperature is defined at 300 K and the core-mantle boundary is defined at 3440 K, which is determined by the reference state (discussed in the next section).

System heating is from the bottom and internal heat sources. In our model, the total internal heating rate is controlled by a reference value, H, and accounts for the internal heating rates representative of regular mantle material and primordial material. To account for the possible enrichment of heat-producing elements (HPEs) in primordial material (e.g., Richter, 1985; Kellogg et al., 1999), we adopt a compositional heating ratio (or enrichment factor), dH_{prim}, that expresses the internal heating rate of thermochemical piles relative to regular mantle material. The internal heating rate of regular mantle material, H_M, (outside of primordial material) is adjusted so that the average internal heating rate of the mantle remains equal to the specified reference value. This internal heating rate is given by

$$H_M = H \times \frac{(1 + C_{total}(dH_{prim} - 1))}{(1 + \bar{C}(dH_{prim} - 1))}, \tag{S1}$$

where C_{total} is the total amount and $\bar{C}$ is the average value of primordial material, respectively. For all calculations, we employ a reference internal heating rate $H = 20$, which corresponds to a dimensional value of 5.44×10^{-12} Wkg^{-1} and an enrichment factor $dH_{prim} = 10$.

Compressibility also generates sinks and sources of heat that are controlled by the dissipation number, Di, which varies radially and is given by

$$\text{Di}(z) = \frac{\alpha_{\text{ref}}(z)gD}{C_P}, \tag{S2}$$

where z is the height above the core-mantle boundary (related to the depth coordinate, d, by $d = D - z$ and the radial coordinate, r, by $r = r_{CMB} + z$, where r_{CMB} is the radius of the core-mantle boundary), $\alpha_{\text{ref}}(z)$ is the reference thermal expansivity

profile, g is the acceleration due to gravity, D is the mantle thickness, and C_P is the heat capacity (which is assumed constant throughout the system). The surface dissipation number is set to $\text{Di}_{\text{surf}} = 1.2$, and the depth variation of thermal expansivity implies a depth average of 0.32.

The fluid properties of the mantle (density, viscosity, thermal diffusivity, and thermal conductivity) are allowed to vary as the system evolves so that the system Rayleigh number is not known *a-priori*. The reference Rayleigh number, Ra, which governs the vigour of convection, is evaluated using the surface values of thermodynamic parameters and reference viscosity, η_{ref}. We prescribe $Ra = 3 \times 10^8$ for all calculations, which results in effective Rayleigh numbers between 10^6 and 5×10^6, depending on the conductivity model.

S2.2 Reference thermodynamical model

Compressible thermochemical convection is characterized by variations relative to a thermodynamic reference state. Reference profiles for the density, temperature, and thermal expansivity are calculated based on the thermodynamic relationships for the Earth's mantle, which are summarized in Tackley (1998). The surface reference temperature, T_{AS}, corresponds to a non-dimensional adiabatic temperature of 0.64 (i.e., a dimensional value of 1600 K). The reference temperature profile represents a geotherm (which corrects for an adiabatic temperature increase) corresponding to T_{AS}. The reference thermal expansivity profile, $\alpha_{\text{ref}}(z)$, decreases by a factor of 5 from surface to core-mantle boundary. The density increases with depth by a factor of approximately 1.5. The Grüneisen parameter, γ, varies with depth such that its product with density is constant. Thermal conductivity is calculated separately and the reference conductivity profile depends on the conductivity model employed (see Methods Section in the main text). The parameters defining this reference state is listed in the Table S1 is illustrated in Figure S1.

S2.3 Thermochemical field

The thermochemical field distinguishes between regular mantle material and a chemically distinct, primordial, material. The primordial material we consider in our models characterizes chemically distinct heterogeneities at the base of the Earth's mantle as a result of early differentiation. The evolution of thermochemical reservoirs is modelled using the tracer ratio method (Tackley & King, 2003). The number of tracers per cell is 40 so that there are just over 10 million tracers in the spherical annulus domain. Tracers are associated with both regular mantle and primordial material and are advected following a 4th order Runge-Kutta method. The compositional field is inferred from the concentration, C, of particles of primordial material in each cell. This field takes on values between 0 for a cell filled with regular material only and 1 for a cell filled with primordial material only. Specifying the exact composition of regular mantle material and primordial material is not needed to calculate the evolution of dense material. Nevertheless, we assume that regular mantle material is pyrolytic and that the primordial material is enriched in iron oxide and bridgmanite.

In our models, the initial distribution of primordial material is contained within a uniform layer on top of the CMB with thickness, h_{DL}, which corresponds to a volume fraction, X_{prim}, by

$$h_{DL} = \frac{[X_{prim}(1 - f^3) + f^3]^{1/3} - f}{1 - f}. \tag{S3}$$

Using $f = 0.55$, the non-dimensional thickness of the dense layer in our model is 0.05514, which corresponds to the bottom 160 km of the lower mantle and a volume fraction of 3%.

Because primordial material is enriched in heavier minerals, it is assumed to be denser than regular (pyrolytic) mantle material. The chemical density contrast between these two materials is characterized by a chemical buoyancy ratio, B, which is defined with respect to the reference density profile and is given by

$$B = \frac{\Delta \rho_C(z)}{\alpha_S \rho_{\text{ref}}(z) \Delta T_S} \tag{S4}$$

We prescribe a value of 0.23, which corresponds to a chemical density contrast, $\Delta \rho_C(z)$, of 95 kgm^{-3} near the surface and 152 kgm^{-3} near the CMB. From this definition of the buoyancy ratio, the chemical density contrast increases with depth

proportionally to the reference density. Compared with models with B defined with respect to the surface density, the buoyancy ratios required for stable chemical stratification will be smaller.

S2.4 Viscosity

Viscosity is modelled using an Arrhenius formulation given by

$$\eta_M(\tilde{d},\tilde{T},C) = \eta_{\text{ref}}[1 + 29H(\tilde{d} - \tilde{d}_{ULM})]\exp\left(V_a\tilde{d} + E_a\frac{1}{\tilde{T} + \tilde{T}_{off}} + \log(\Delta\eta_C)C\right). \tag{S5}$$

Depth- dependence is characterized by a viscosity contrast of 10^2 across the mantle depth (corresponding to a logarithmic vertical viscosity ratio $V_a = 2.3026$). An additional viscosity jump by a factor of 30 is imposed at the 660-km boundary (with non-dimensional depth given by $\tilde{d}_{ULM} = 0.22837$) to account for a phase change (expressed by the Heaviside function in Equation S5). Temperature- dependence is characterized by a thermal viscosity contrast of 10^7 (corresponding to a logarithmic thermal viscosity ratio $E_a = 16.118$). The parameter $\tilde{T}_{off}$ is a temperature offset, which is added to the temperature to reduce the viscosity contrast across the top thermal boundary layer. In this study, $\tilde{T}_{off} = 0.90$. A factor of 30 viscosity contrast ($\Delta\eta_C$) is imposed between lower mantle material and thermochemical reservoirs because dense material enriched in bridgmanite (Trampert et al., 2004; Mosca et al., 2012) is assumed to be more viscous (Yamazaki & Karato, 2001).

A yield stress, σ_0, of 290 MPa is imposed at the surface so that the development of a stagnant-lid is avoided. The yield viscosity is defined from the yield stress $\sigma_Y = \sigma_0 + \dot{\sigma}_z P$ and the second invariant of the stress tensor, $\dot{e}$, and is given by

$$\eta_Y = \frac{\sigma_0 + \dot{\sigma}_z P}{2\dot{e}}. \tag{S6}$$

The total viscosity then is given by

$$\eta = \frac{1}{\frac{1}{\eta_M} + \frac{1}{\eta_Y}} \tag{S7}$$

Finally, viscosity is truncated so that non-dimensional viscosity values do not fall below 10^{-3} or exceed 10^5.

S2.5 Phase changes

The transformation of ringwoodite into bridgmanite and ferropericlase at 660 km is modelled with a discontinuous phase transition controlled by defining a point on the phase boundary and a Clapeyron slope, Γ_{660}. Here, the anchor point is set at $d = 660$ km and $T = 1900$ K, and the Clapeyron slope is set to $\Gamma_{660} = -2.5$ MPaK^{-1}. The accompanying density contrast is fixed to $\Delta\rho_{660} = 400$ kgm^{-3} and is scaled with the surface density. Combined with the 660-km viscosity increase (from upper to lower mantle), the 660-km phase change has a strong influence on the geometry of the plumes. This transition acts as a negatively buoyant barrier, which results in a spreading of the plume conduit beneath this boundary, and a thinning above it. Further phase changes in the lowermost mantle from perovskite to post-perovskite is neglected.

S2.6 Initial conditions

The initial condition for the temperature field is based on an adiabatic temperature of 2000 K with surface and core-mantle boundary layer thicknesses of approximately 30 km. Random temperature perturbations with an amplitude of 125 K are uniformly distributed throughout the domain. Under this setup, an initial transient phase lasting approximately 1.0 to 2.0 Gyr is observed (depending on the conductivity model employed) where the bottom of the mantle heats up and the first downwellings impinge on the initial dense layer.

Simulations are computed over a non-dimensional time of 0.0318. Dimensionalizing using the diffusion timescale (D^2/κ_S), results in a total of 11.2 Gyr. The longer simulation time is necessary to allow the simulations' heat flows to achieve a quasi-steady state. It is possible that significant developments during the long-term evolution of thermochemical material may occur

over timescales comparable to or longer than the age of the solar system. We point out that our models are not designed to model the detailed evolution of the Earth's mantle, for which accurate initial conditions are not yet known. Instead, our models aim to identify the thermochemical structure and its evolution as a function of the system's conductivity model.

S3 Derived quantities and statistics on observed physical parameters

S3.1 Adiabatic correction and rescaling to Earth's mantle

The energy and momentum equations are solved with the temperature field that has been corrected for adiabatic effects. However, for practical reasons, the output temperature field states are saved as the uncompressed temperature, which excludes these effects. In all figures that present temperature fields, plume and downwelling contours, or temperature profiles (Figures 2 - 6 in the main text and Supplement Figures S2 - S10,S14 - S17), temperature has been rescaled and corrected with the adiabatic increase of temperature with pressure. The dimensional temperature field, $T(r,\phi)$, is obtained from the non-dimensional, uncompressed temperature field, $\tilde{T}(r,\phi)$, following

$$\Theta(r,\phi) = [\tilde{T}(r,\phi) + \tilde{T}_{top}] \times \Delta T_S \tag{S8}$$

where $\Theta(r,\phi) = T(r,\phi)/a(z)$ is the potential temperature, $\Delta T_S = 2500$ K is the superadiabatic temperature difference, $\tilde{T}_{top}$ is the non-dimensional surface temperature, which is fixed to 0.12 and corresponds to a surface temperature $T_{surf} = 300$ K, and $a(z)$ is the adiabatic correction at height z above the core-mantle boundary. The adiabatic correction is given by

$$a(z) = \exp\left[\int_0^z \text{Di}_{surf} \frac{\alpha_{ref}(z')}{C_{Pref}(z')} dz'\right] \tag{S9}$$

where Di_{surf} is the surface dissipation number, and $\alpha_{ref}(z)$ and $C_{Pref}(z)$ are the thermodynamic reference thermal expansivity and heat capacity, respectively. The adiabatic correction varies from 1.0 at the surface to about 1.40 at the CMB.

S3.2 Definition of mantle structures

Mantle structures, namely thermal upwellings and downwellings, are indicated in the various field snapshots we present in our figures. These structures can be particularly helpful when the field shows no discernible variations that might indicate flow (i.e., a constant or radially varying conductivity field). The contour of an upwelling characterizes mantle plumes and similarly, the contour of a downwelling characterizes subducting slabs. We adapt the definition of thermal structures based on the formalism by Labrosse (2002). Here, the plume region is defined as regions where the temperature exceeds the horizontally averaged temperature, $\bar{T}(z)$, by a fraction of c_{plume} of the maximum excess temperature anomaly. That is, regions where temperature is given by

$$T_{plume}(z) \geq \bar{T}(z) + c_{plume}[T_{max}(z) - \bar{T}(z)], \tag{S10}$$

where $T_{max}(z)$ is the maximum temperature. Downwelling regions are defined similarly and given by

$$T_{slab}(z) \leq \bar{T}(z) + c_{slab}[T_{min}(z) - \bar{T}(z)], \tag{S11}$$

where $T_{min}(z)$ is the minimum temperature. The values of c_{plume} and c_{slab} are subjective and decreasing these constants increase the regions they characterize. In this study, both c_{plume} and c_{slab} are set to 0.5 so that the regions are defined by half the magnitude of the difference between the temperature anomaly and the horizontal average.

Thermochemical piles are defined by a threshold value of C. In our calculations, we define thermochemical piles as having C larger than 0.9. The higher threshold value means that piles, as their name suggests, are the densest material that pool on top of the CMB. Even the densest material in our calculations exhibit greater extension above the CMB. Furthermore, a lower threshold value for thermochemical material may result in estimates of the mean pile temperature that are offset by cooler and lighter material.

5

S3.3 Derived quantities

170   In this study, all observable physical parameters are averaged over a 2 Gyr window centred about $t = 4.5$ Gyr (illustrated in Figure 7 and are presented in Table 1 in the main text). We derive some additional physical parameters such as average height and the mean density anomalies of primordial material below.

The average height of primordial material, h_C, is considered as an indication of efficient mixing of primordial material in the mantle. This height is calculated using a volumetric integral weighted by the concentration of primordial material,

$$175 \quad h_C = \int_V (r - r_{CMB}) C(r,\phi) dV \Big/ \int_V C(r,\phi) dV. \tag{S12}$$

Average height of primordial material is bound from below by a minimum value, $h_{C,min} = h_{dl}/2$, where h_{dl} is the initial thickness of the thermochemical reservoir, and bound from above by a maximum value (when primordial material is completely mixed) is given by

$$h_{C,max} = D \times \frac{\left(\frac{1+f^3}{2}\right)^{1/3} - f}{1 - f}. \tag{S13}$$

180   Here, $h_{C,min} = 80$ km and $h_{C,max} = 1830$ km. We also consider other mean heights of primordial material for $C(r,\phi)$ within specific ranges. Minor enrichment of dense material with $C(r,\phi) \leq 0.02$ is useful for monitoring the onset of slow mixing of primordial material into regular mantle material. A moderate enrichment of dense material with $C(r,\phi) \leq 0.90$ and > 0.02 is useful for monitoring the rapid entrainment of primordial material. This value range characterizes a thin veneer of primordial material with $C(r,\phi) \leq 0.90$ that surrounds the thermochemical reservoirs. The rapid uplift of this material typically precedes

185   the onset of entrainment. Finally, dense material with $C(r,\phi) > 0.90$ characterizes the thermochemical piles. While some of this material can be rapidly entrained, the bulk concentration will be localized near the CMB. The timing of the onset of the entrainment of dense material, $t_{inst.}$, can be computed from the timing of the maximum of the second derivative of $h_{C \leq 0.9}$ and is confirmed by observing the deviation of $h_{C \leq 0.9}$ from $h_{C \geq 0.9}$ or h_C from $h_{C \geq 0.9}$.

The density anomalies of primordial material, $(d\rho/\rho)_{z,prim}$, are calculated relative to the horizontally averaged density. At

190   each depth in the mantle, the density difference of the primordial field is calculated ($d\rho = \rho_{prim} - \bar{\rho}_z$). The average density anomaly is calculated with respect to the density value of each point at a given depth so that

$$(d\rho/\rho)_{z,prim} = \int_{S_z} \frac{\rho_{prim} - \bar{\rho}_z}{\rho_{prim}} dS_z \Big/ \int_{S_z} dS_z. \tag{S14}$$

Monitoring the density profile of primordial material clarifies its distribution throughout the mantle depth. In conjunction with the evolution of average heights, the regions of dense material enrichment is further clarified.

Parameter	Symbol	Value	Units	Non-dimensional
Governing parameters				
Reference Rayleigh number	Ra			3.0×10^8
Surface dissipation number	Di_{surf}			1.2
Total internal heating	H	5.44×10^{-12}	(Wkg^{-1})	20
Compositional heating ratio	dH_{prim}			10
Compositional parameters				
Buoyancy ratio	B			0.23
Volume fraction of dense material (%)	X_{prim}			3%
Thickness of initial dense layer	h_{DL}			0.05514
Physical & thermodynamical parameters				
Acceleration of gravity	g	9.81	(ms^{-2})	1
Mantle thickness	D	2891	(km)	1
Reference adiabat	T_{AS}	1600	(K)	0.64
Super-adiabatic temperature difference	ΔT_S	2500	(K)	1
Surface density	ρ_S	3300	(kgm^{-3})	1
Surface thermal expansion	α_S	5.0×10^{-5}	(K^{-1})	1
Surface thermal diffusivity	κ_S	7.5×10^{-7}	(m^2s^{-1})	1
Heat capacity	C_P	1200	$(Jkg^{-1}K^{-1})$	1
Surface conductivity	k_S	3	$(Wm^{-1}K^{-1})$	1
Surface Grüneisen parameter	γ_S			1.091
Density jump at z = 660 km	$\Delta\rho_{660}$	400	(kgm^{-3})	0.1212
Clapeyron slope at z = 660 km	Γ_{660}	-2.5	$(MPaK^{-1})$	-0.0668
CMB temperature	T_{CMB}	3440	(K)	1.376
Density jump at CMB	$\Delta\rho_{CMB}$	5280	(kgm^{-3})	1.6
Conductivity Parameters				
Depth- dependence contrast	K_D			1.0 - 10.0
Temperature- dependence exponent	n			0.0, 0.5, 0.8
Compositional correction	K_C			0.5 - 1.0
Viscosity Law				
Reference viscosity	η_{ref}	4.346×10^{20}	Pa $\cdot$ s	1
Viscosity ratio at z = 660 km	$\Delta\eta_{660}$			30
Logarithmic thermal viscosity ratio	$E_a (= \log(\Delta\eta_T))$			16.118
Logarithmic vertical viscosity ratio	$V_a (= \log(\Delta\eta_D))$			2.3026
Compositional viscosity ratio	$\Delta\eta_C$			30
Surface yield stress	σ_0	290	(MPa)	7.5×10^6
Yield stress gradient	$\dot{\sigma}_z$	0.01	$(PaPa^{-1})$	0.01

Table S1. Parameters and dimensional scales for our thermochemical mantle convection model.

Table S2. Averaged properties for all cases presented. Supplemental cases are indicated by a letter 'S'. Except for $t_{inst.}$, all values are computed within in a 2 Gyr period encompassing $t = 9.0$ Gyr.

Case #	K_D	K_C	n	T_{mean} (K)	T_{prim} (K)	global rms dT_{prim} (K)	negative rms dT_{prim} (K)	positive rms dT_{prim} (K)	$\Delta T_{prim,max}$ (K)	Q_{SURF} (TW)	Q_{CMB} (TW)	h_C (km)	A_{CMB}(%)	$t_{inst.}$ (Gyr)
1	1	1	0	2040	4020	640	620	670	1360	25.5	3.6	660	36	5.8
2	2.5	1	0	2110	3900	410	320	500	1120	29.0	5.8	230	38	9.2
3	2.5	1	0.5	2340	4180	770	750	790	1600	25.6	3.3	1070	19	5.2
4	2.5	0.8	0.5	2360	4010	820	750	890	1850	24.8	3.2	1120	23	4.9
5	2.5	0.5	0.5	2370	4270	910	900	920	1920	24.9	3.3	1090	20	4.5
6	2.5	1	0.8	2530	4230	950	880	1020	1950	22.0	1.9	1300	20	4.5
7	5	1	0	2190	3540	160	140	180	430	31.9	9.8	200	43	> 11.2
8	10	1	0	2290	3420	100	120	90	240	37.1	15.8	200	43	> 11.2
9	10	1	0.5	2350	3860	440	330	570	1220	27.6	4.2	220	47	> 11.2
10	10	0.8	0.5	2360	4020	580	450	740	1570	31.4	6.1	430	32	8.4
11	10	0.5	0.5	2380	4020	580	450	720	1740	28.2	5.1	310	46	9.0
12	10	1	0.8	2500	4080	650	500	830	1810	23.6	1.8	440	53	8.2
13	9.185	1	0	2210	3410	90	120	70	170	37.2	15.0	180	47	> 11.2
14	9.185	0.8	0	2230	3460	120	120	120	300	37.9	16.0	200	41	> 11.2
15	9.185	1	0.5	2350	3790	350	260	460	1060	26.7	4.3	190	47	> 11.2
16	9.185	0.8	0.5	2340	3900	410	320	510	1140	26.3	4.1	200	45	11.1
17	9.185	0.5	0.5	2370	4110	590	460	740	1650	26.7	5.4	280	41	8.8
18	9.185	0.8	0.8	2470	4160	680	540	850	1840	24.3	3.0	680	37	6.6
S1	1	1	0.5	2360	4290	940	920	970	1890	23.9	2.1	1490	10	3.9
S2	1	1	0.8	2550	4340	930	910	940	1870	23.9	1.5	1640	5	4.1
S3	5	1	0.5	2360	4110	590	490	710	1450	24.8	3.1	510	38	6.0
S4	5	1	0.8	2500	4430	740	690	800	1530	24.1	2.7	1030	23	5.4
S5	5	0.8	0.5	2370	4080	710	590	870	1810	25.3	3.2	610	42	5.6
S6	5	0.5	0.5	2380	4280	650	590	720	1550	27.4	4.6	920	24	5.2

8

Table S3. Averaged properties for all cases presented. Supplemental cases are indicated by a letter 'S'. Except for $t_{inst.}$, all values are computed from $t = 3.0$ to 11.2 Gyr.

Case #	K_D	K_C	n	T_{mean} (K)	T_{prim} (K)	global rms dT_{prim} (K)	negative rms dT_{prim} (K)	positive rms dT_{prim} (K)	$\Delta T_{prim,max}$ (K)	Q_{SURF} (TW)	Q_{CMB} (TW)	h_C (km)	A_{CMB}(%)	$t_{inst.}$ (Gyr)
1	1	1	0	2080	3950	560	510	620	1400	26.6	2.1	420	53	5.8
2	2.5	1	0	2150	3790	350	280	430	980	29.5	5.1	210	45	9.2
3	2.5	1	0.5	2350	4120	710	660	770	1600	24.5	1.8	720	42	5.2
4	2.5	0.8	0.5	2370	4120	770	700	840	1710	24.3	2.2	840	36	4.9
5	2.5	0.5	0.5	2370	4230	840	790	890	1910	24.4	2.3	860	39	4.5
6	2.5	1	0.8	2520	4340	850	780	930	1890	22.0	1.0	940	34	4.5
7	5	1	0	2210	3530	160	140	180	420	32.4	9.4	190	45	> 11.2
8	10	1	0	2290	3420	100	120	90	220	37.1	15.4	190	45	> 11.2
9	10	1	0.5	2370	3810	370	280	470	1020	27.4	4.1	200	50	> 11.2
10	10	0.8	0.5	2380	3950	490	390	620	1290	28.9	5.4	320	39	8.4
11	10	0.5	0.5	2390	3900	460	380	560	1370	26.6	4.4	240	51	9.0
12	10	1	0.8	2500	4060	590	450	740	1570	22.5	1.3	290	57	8.2
13	9.185	1	0	2230	3410	90	120	70	160	37.5	14.7	180	48	> 11.2
14	9.185	0.8	0	2240	3460	120	120	120	290	38.0	15.6	200	41	> 11.2
15	9.185	1	0.5	2360	3720	280	220	360	840	26.5	4.0	180	52	> 11.2
16	9.185	0.8	0.5	2350	3830	360	280	440	990	26.5	4.0	180	51	11.1
17	9.185	0.5	0.5	2370	3990	510	400	640	1420	26.3	4.3	230	50	8.8
18	9.185	0.8	0.8	2470	4220	630	530	730	1540	23.9	2.4	480	42	6.6
S1	1	1	0.5	2370	4390	860	850	880	1680	24.0	1.7	1230	20	3.9
S2	1	1	0.8	2540	4550	870	840	910	1910	22.2	1.0	1350	18	4.1
S3	5	1	0.5	2380	4090	560	460	680	1460	25.0	2.6	390	43	6.0
S4	5	1	0.8	2490	4390	720	660	780	1560	22.8	1.6	700	39	5.4
S5	5	0.8	0.5	2380	4090	640	540	760	1580	25.4	3.0	490	42	5.6
S6	5	0.5	0.5	2390	4240	670	590	760	1580	25.9	3.5	630	40	5.2

Table S4. Averaged properties for case no. 17 (K_{DH}, $n = 0.5$, and $K_C = 0.5$) run with different initial conditions. Except for $t_{inst.}$, all values are computed within in a 2 Gyr period encompassing $t = 4.5$ Gyr.

Case	T_{init} (K)	dT (K)	T_{mean} (K)	T_{prim} (K)	global rms dT_{prim} (K)	negative rms dT_{prim} (K)	positive rms dT_{prim} (K)	$\Delta T_{prim,max}$ (K)	Q_{SURF} (TW)	Q_{CMB} (TW)	h_C (km)	A_{CMB} (%)	$t_{inst.}$ (Gyr)
Reference IC	2000	125	2380	3820	420	320	520	1110	25.6	3.0	160	64	8.8
Cooler IC	1750	125	2240	3720	320	280	360	910	22.8	3.7	160	63	9.7
Hotter IC	2250	125	2480	3990	490	390	600	1130	29.5	3.9	200	53	6.4
Reference IC, bigger perturbation	2000	375	2360	3770	350	300	400	950	25.8	3.0	160	63	9.0
Hotter IC, bigger perturbation	2250	375	2490	4020	520	400	670	1300	29.9	4.1	210	48	6.0
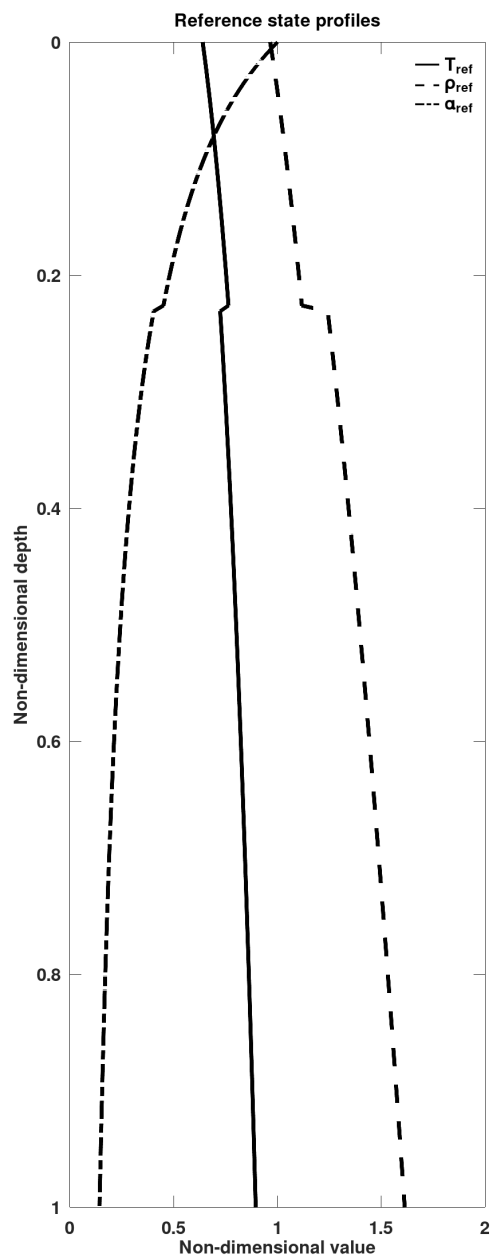
Figure S1. Radial profiles for adiabatic temperature, density, and thermal expansivity indicate the reference state for each calculation.
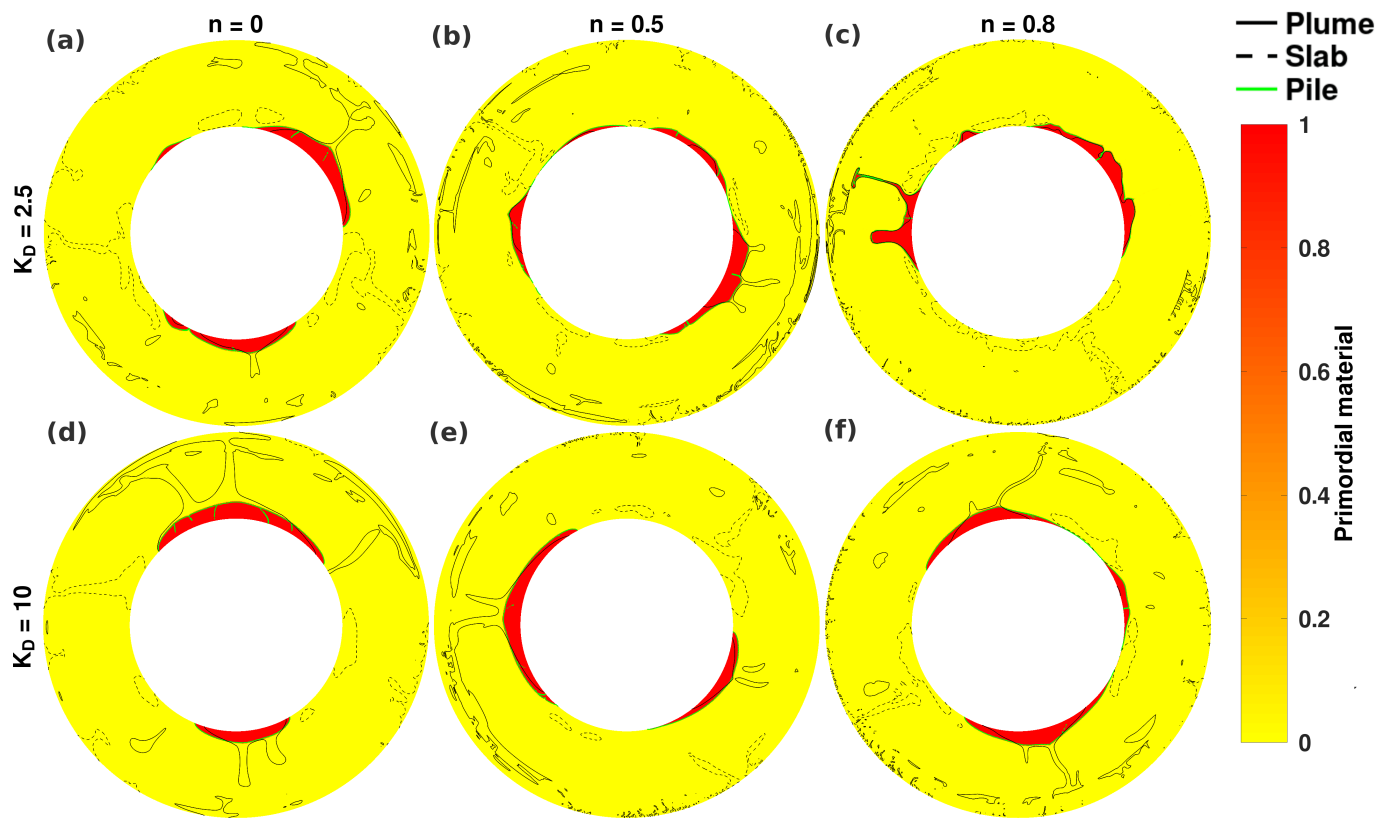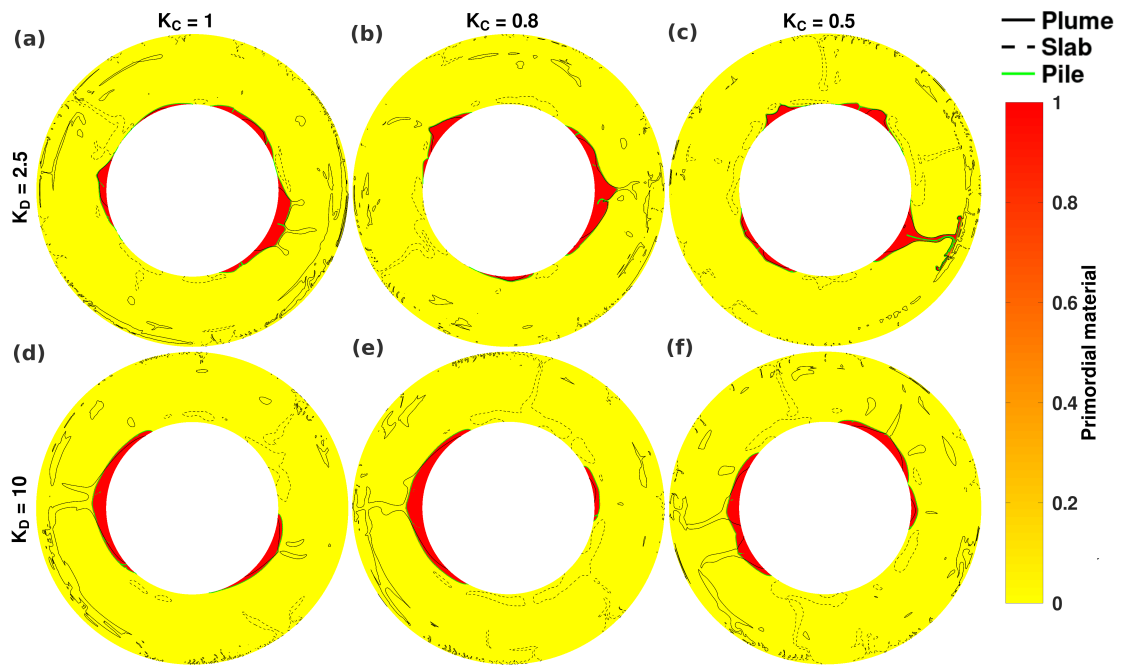
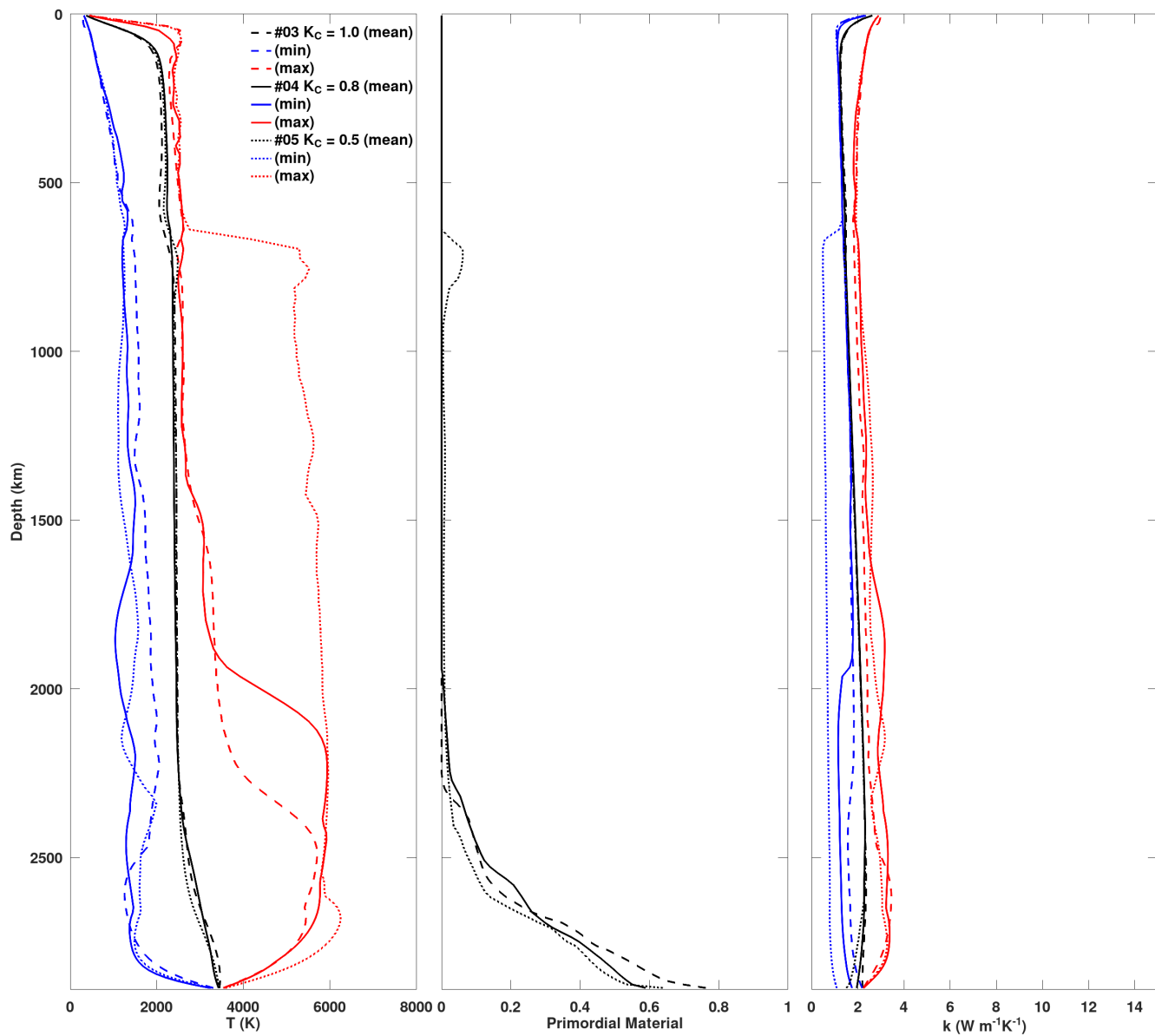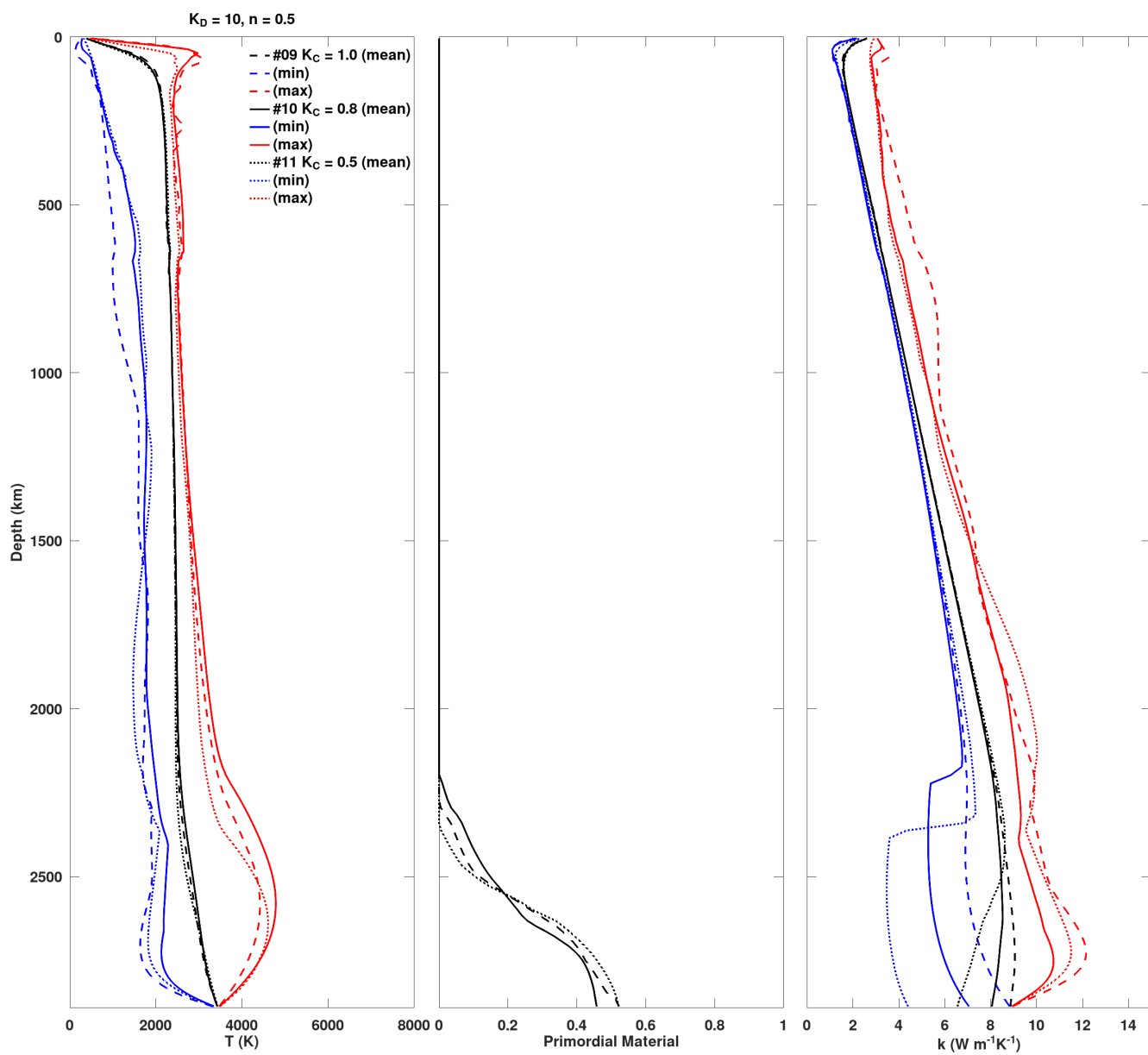**Figure S2.** Primordial material field snapshots corresponding to cases presented in Figure 4.
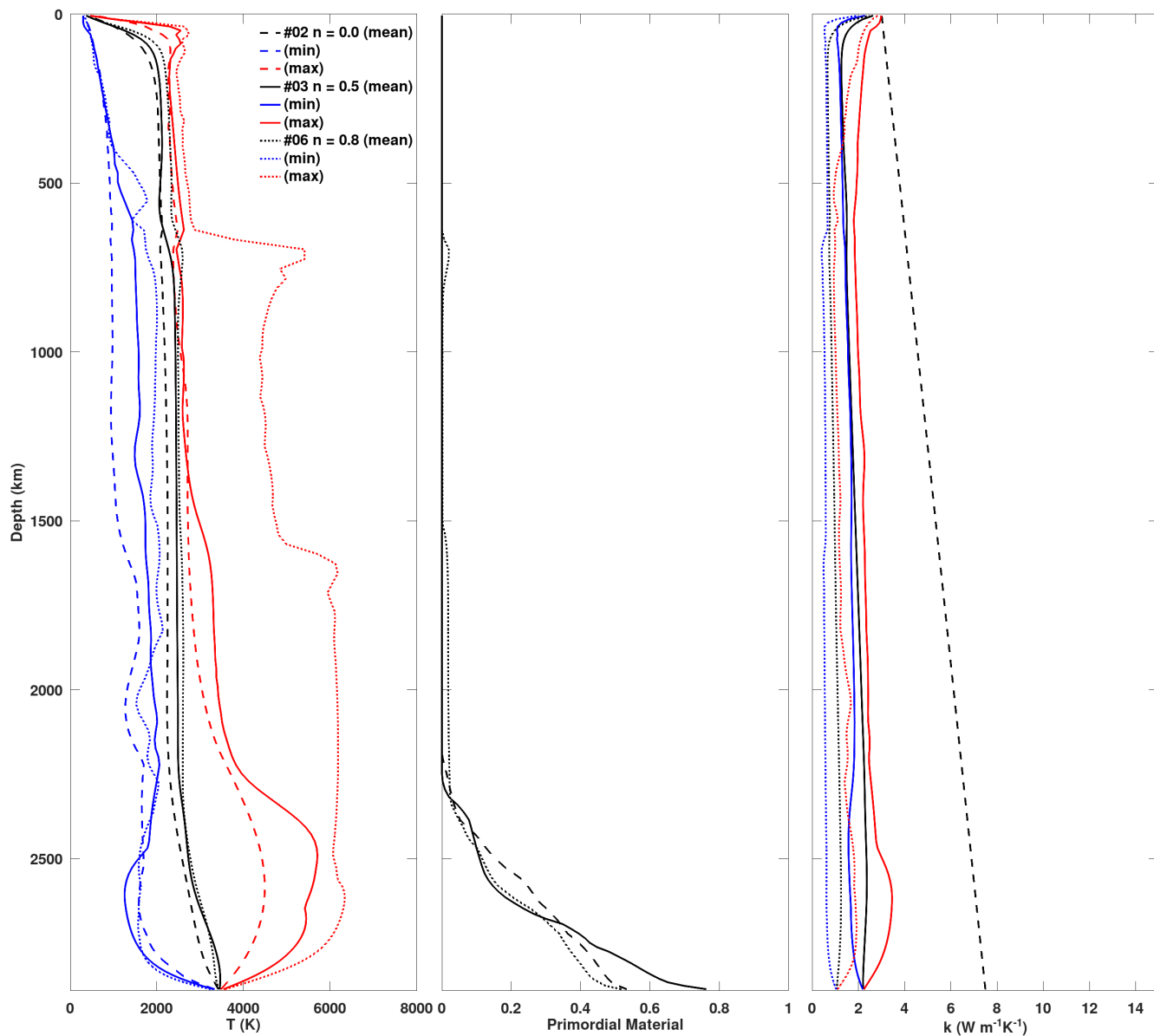
Figure S3. Mean temperature, primordial material, and composition profiles corresponding to cases featuring $K_D = 2.5$ presented in Figure 4. Case number is indicated in the legend and each case corresponds to a unique line style (dashed-, solid-, or dotted- curves). The profiles for the mean, minimum, and maximum are indicated by black, blue, and red curves, respectively.
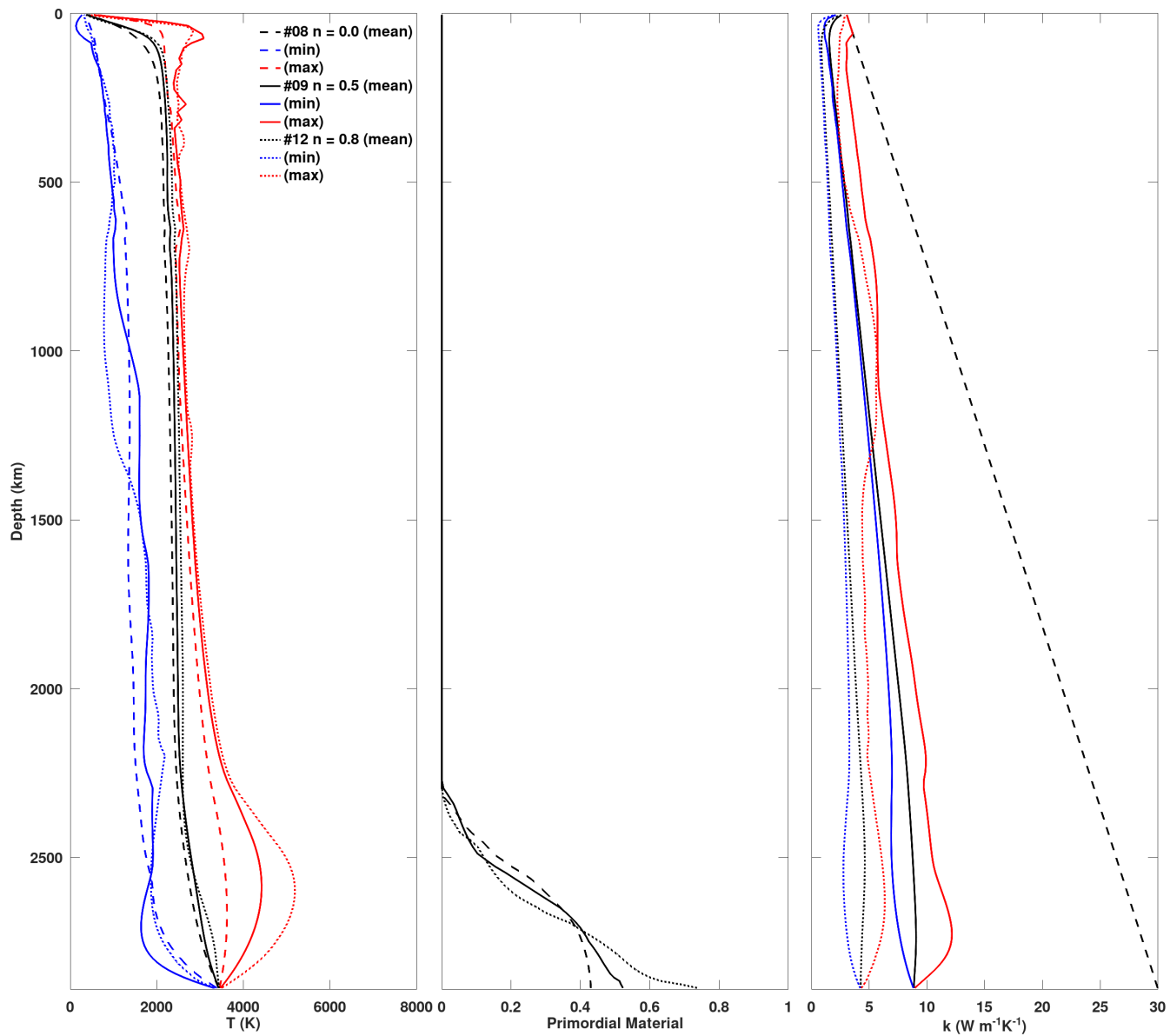
Figure S4. Mean temperature, primordial material, and composition profiles corresponding to cases featuring $K_D = 10$ presented in Figure 4. Profiles are defined similarly as in Figure S3.
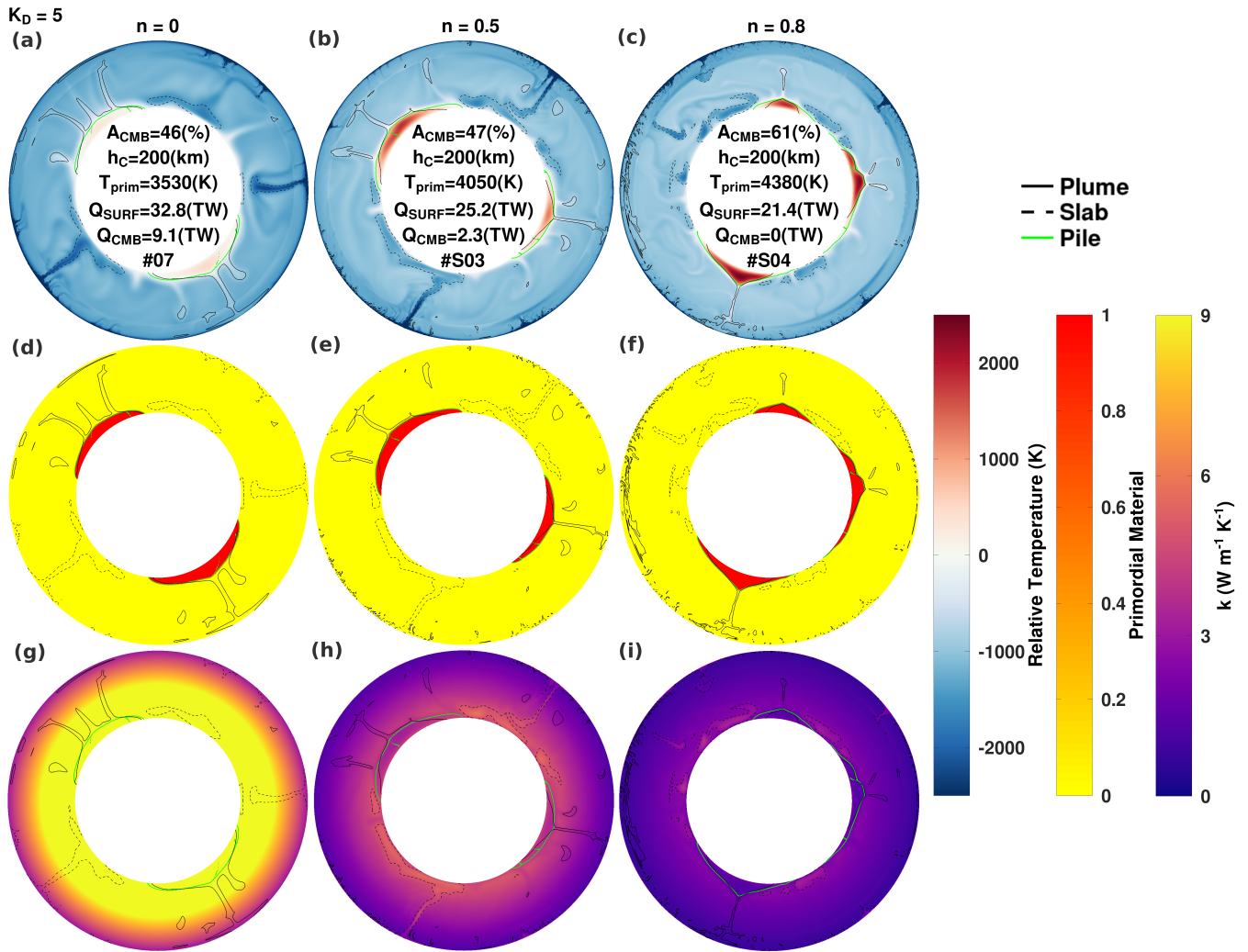
Figure S5. Temperature (top row), primordial material (centre row), and conductivity fields (bottom row) featuring $K_D = 5$ and increasing temperature- dependence, n. Contours are indicated in the legend and field values are indicated on the colour bars. The conductivity colour bar saturates at $9\ \mathrm{Wm^{-1}K^{-1}}$ so that the values in (g) may be larger. Averaged properties and case numbers are inset.

Figure S6. Primordial material field snapshots corresponding to cases presented in Figure 5.

Figure S7. Mean temperature, primordial material, and composition profiles corresponding to cases featuring $K_D = 2.5$ presented in Figure 5. Profiles are defined similarly as in Figure S3.

Figure S8. Mean temperature, primordial material, and composition profiles corresponding to cases featuring $K_D = 10$ presented in Figure 5. Profiles are defined similarly as in Figure S3.
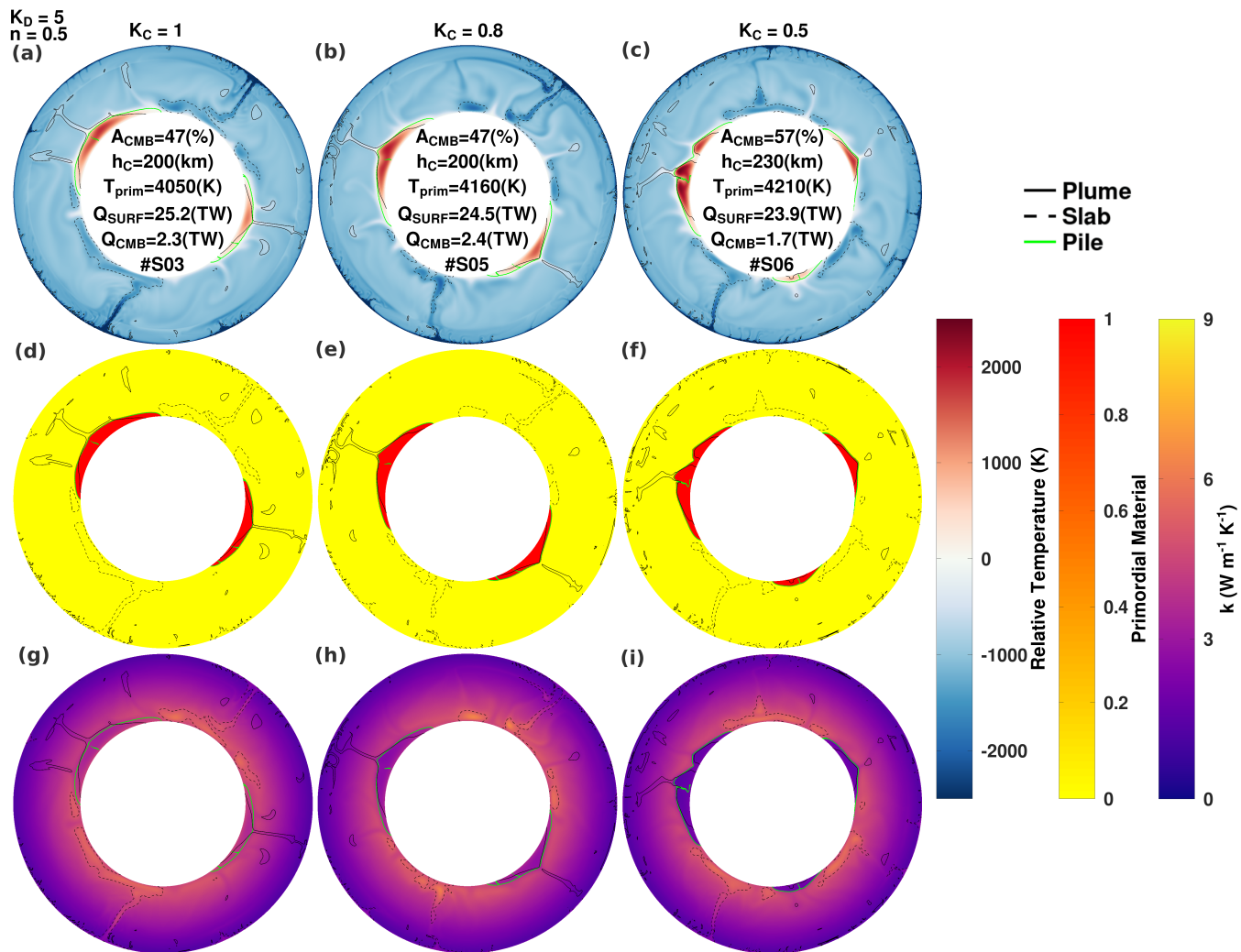
Figure S9. Temperature (top row), primordial material (centre row), and conductivity fields (bottom row) featuring $K_D = 5$ and $n = 0.5$ with increasing composition- dependence (decreasing K_C). Averaged properties and case numbers are inset.
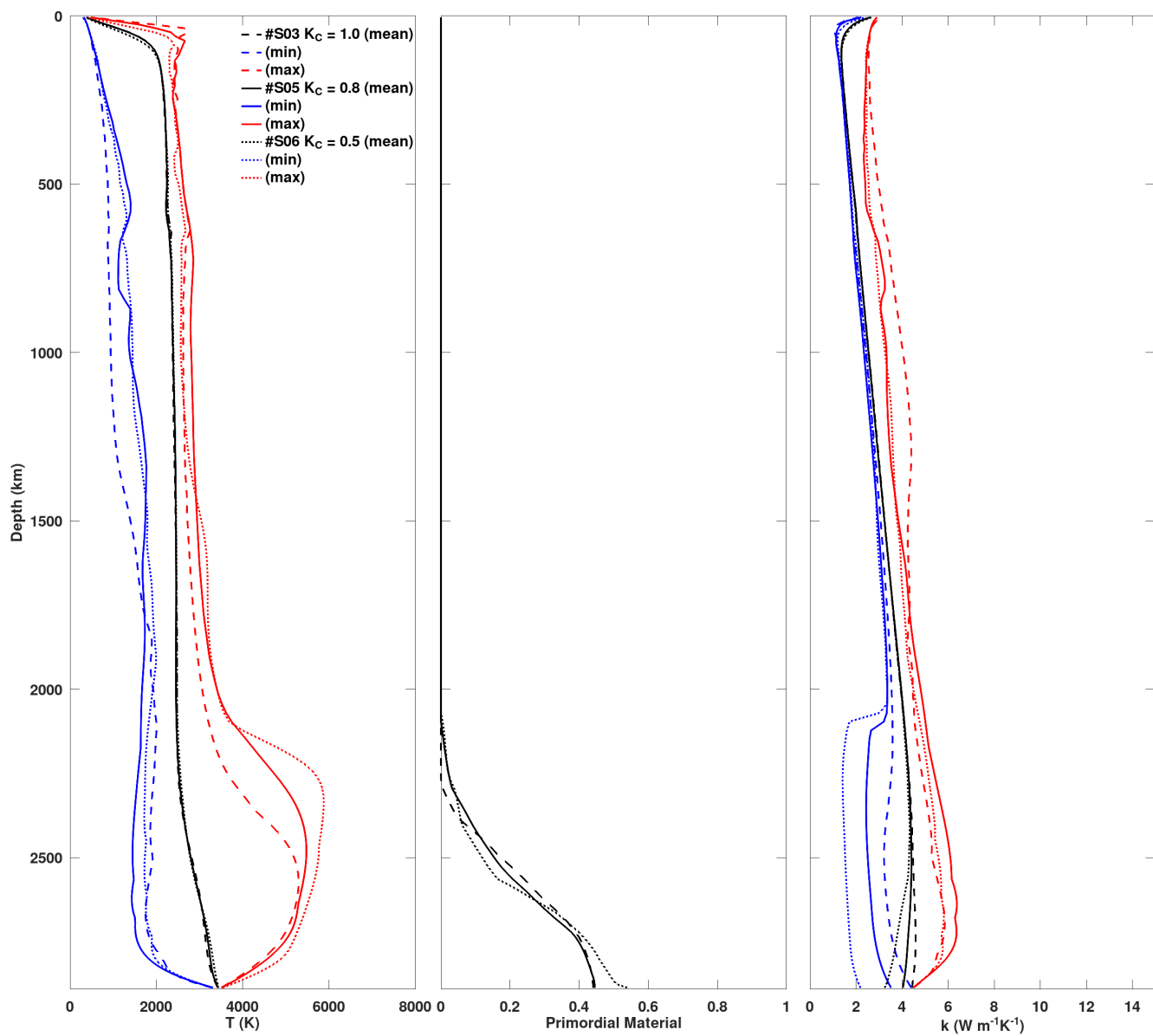
Figure S10. Mean temperature, primordial material, and composition profiles corresponding to cases in Figure S9. Profiles are defined similarly as in Figure S3.
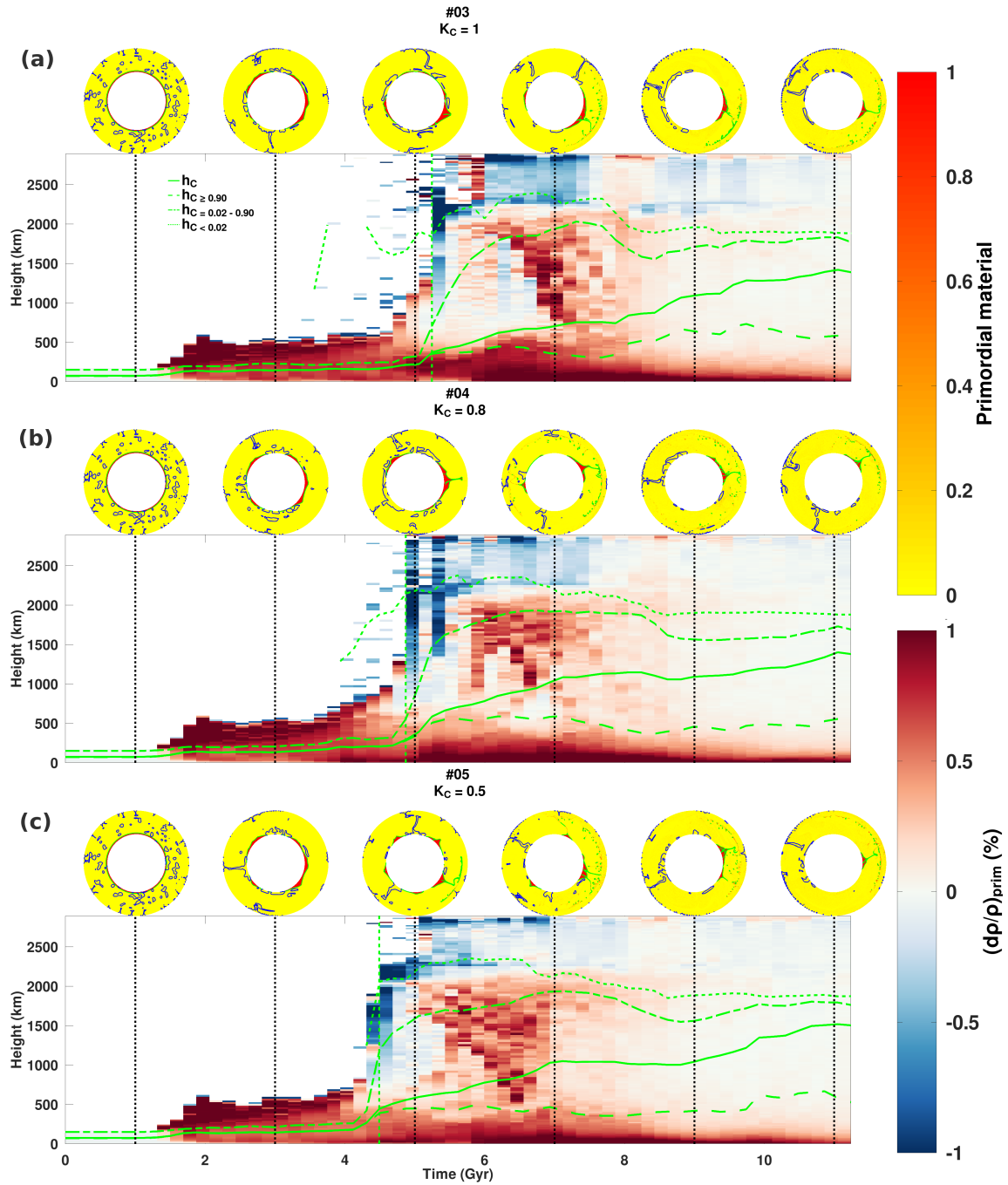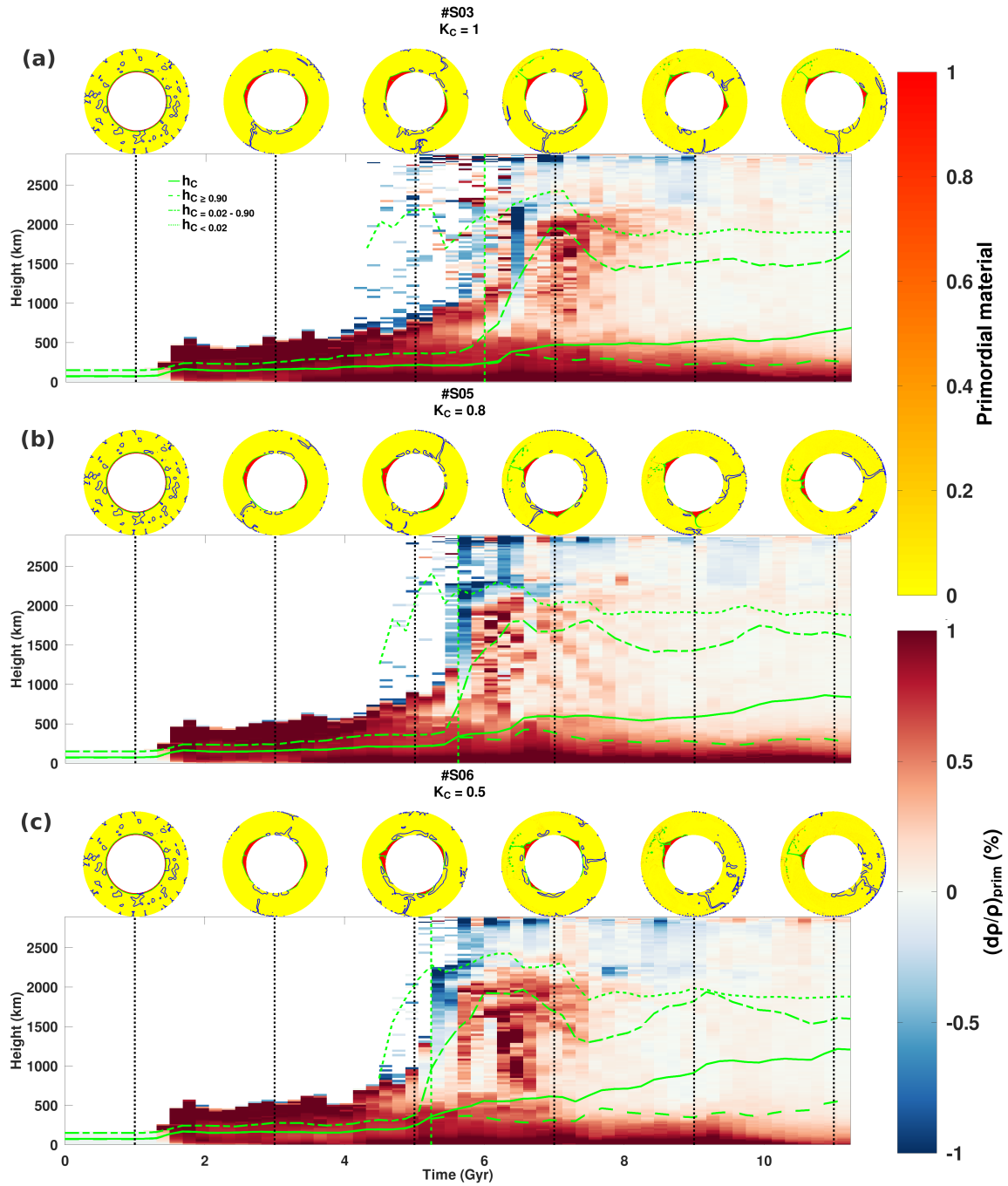
Figure S11. Evolution of the horizontally averaged primordial material density anomalies is illustrated for cases featuring $K_D = 2.5$ and $n = 0.5$ with increasing composition- dependence (decreasing K_C). Primordial field snapshots are sampled at 2 Gyr intervals starting at $t = 1$ Gyr above the timeseries (dashed-black vertical line indicates the time). Mean heights of primordial material are plotted on top of the density anomaly timeseries. The dashed-green vertical line indicates the onset of instability in thermochemical reservoirs. In the snapshots, downwelling structures are indicated by solid blue contours and piles are indicated by solid green contours.
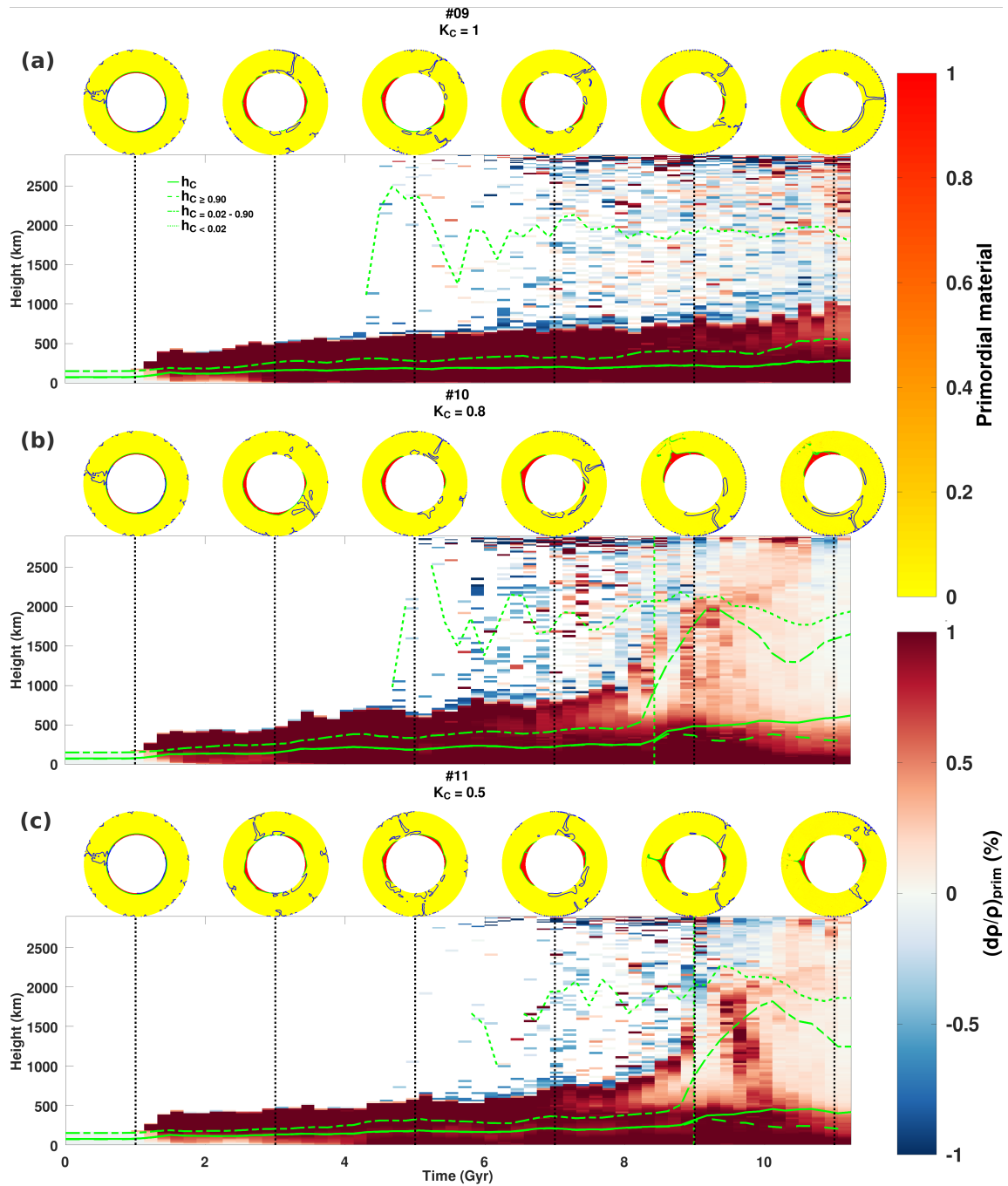
Figure S12. Evolution of the horizontally averaged primordial material density anomalies is illustrated for cases featuring $K_D = 10$ and $n = 0.5$ with increasing composition- dependence (decreasing K_C).

Figure S13. Evolution of the horizontally averaged primordial material density anomalies is illustrated for cases featuring $K_D = 5$ and $n = 0.5$ with increasing composition- dependence (decreasing K_C).
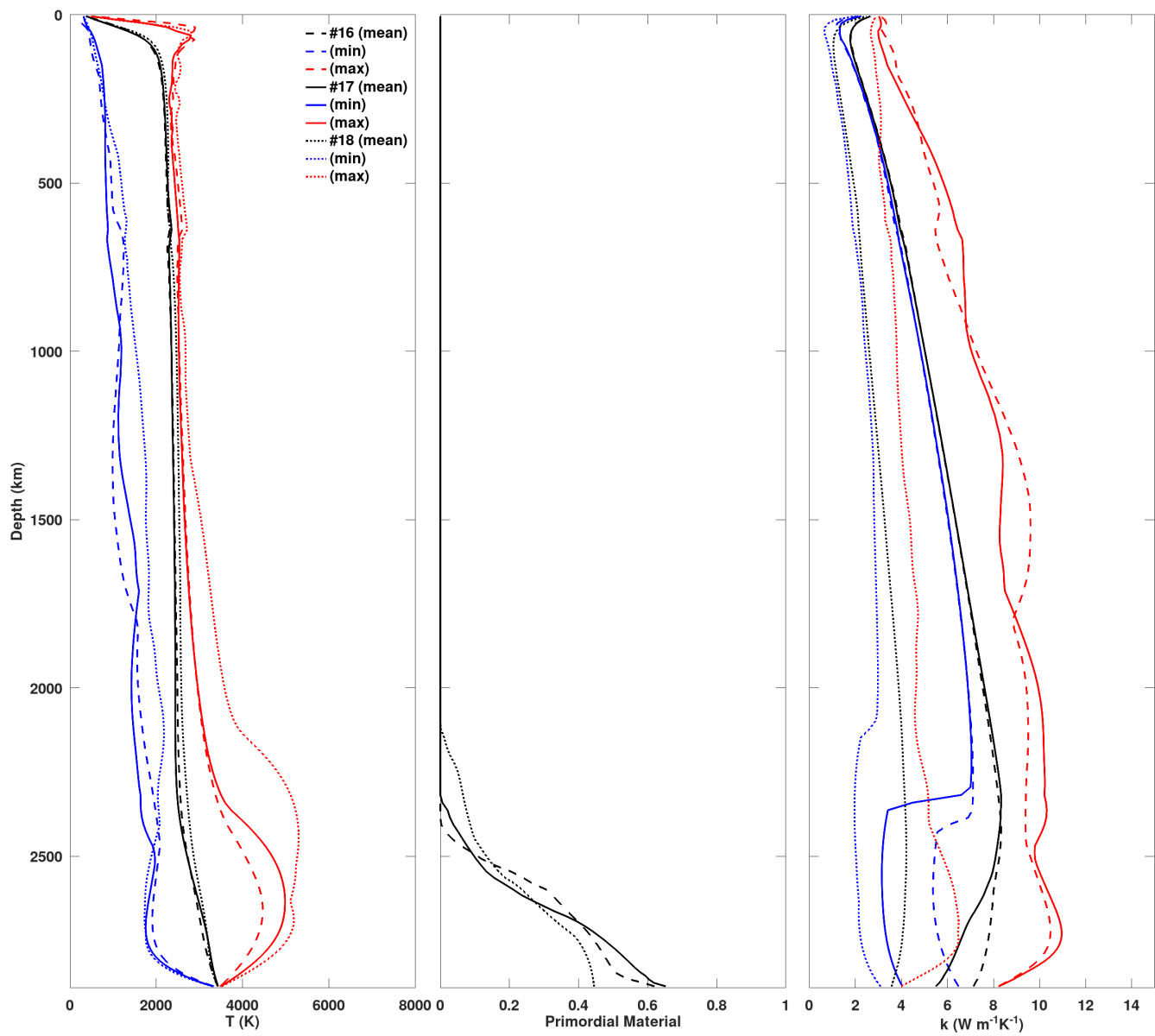
Figure S14. Mean temperature, primordial material, and composition profiles corresponding to cases in Figure 8 and 9. Profiles are defined similarly as in Figure S3.
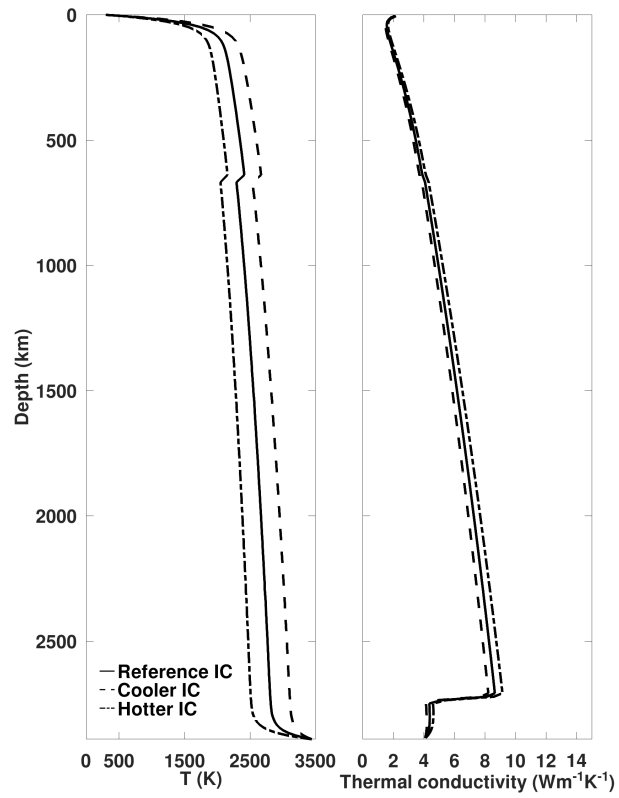
Figure S15. Initial temperature profiles (left panel) and initial conductivity profiles (right panel) for case no. 17 with different initial temperatures.
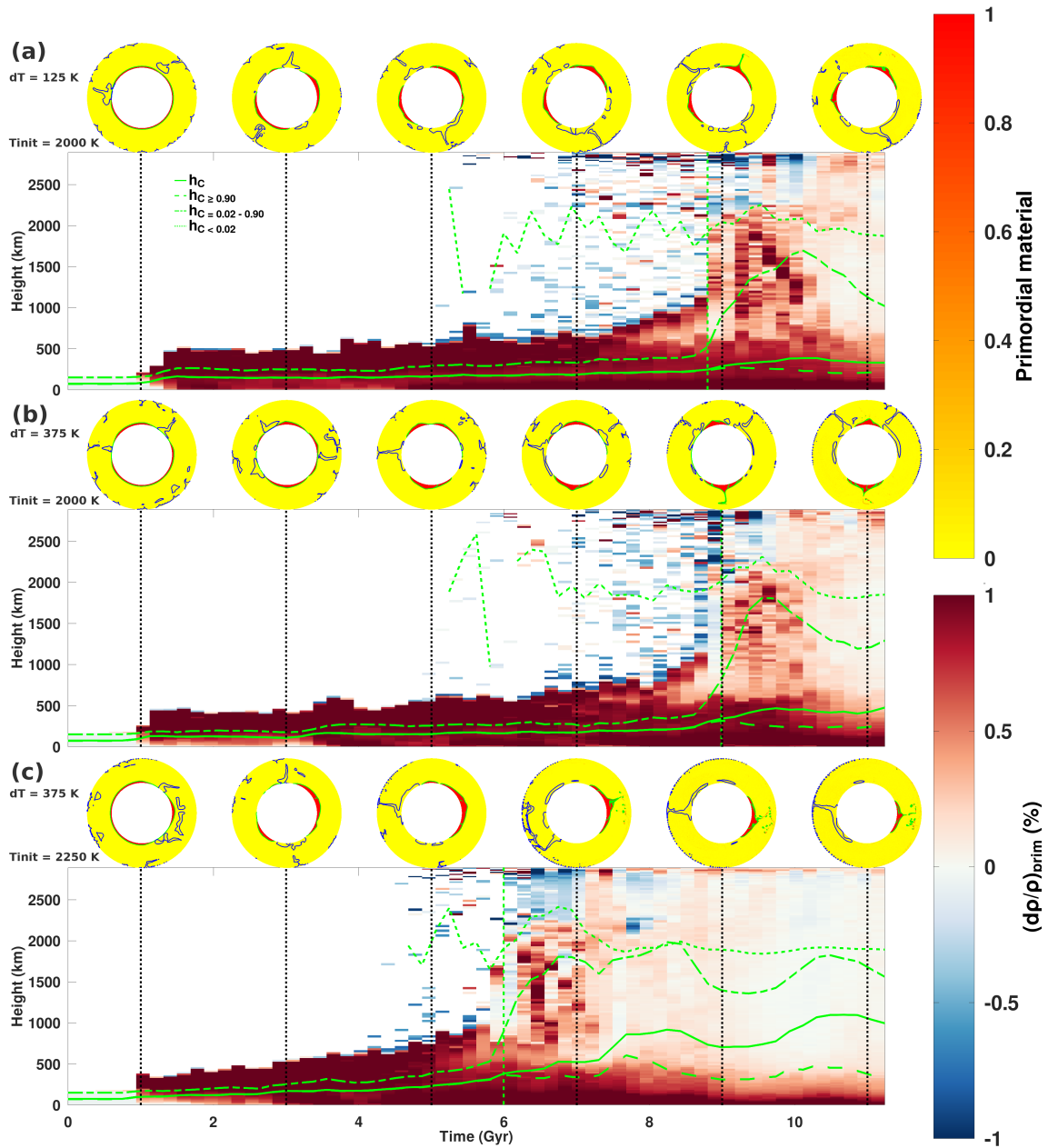
Figure S16. Evolution of the horizontally averaged primordial material density anomalies is illustrated for case no. 17 with different initial temperature, T_{init}, and initial temperature perturbation amplitude, dT.
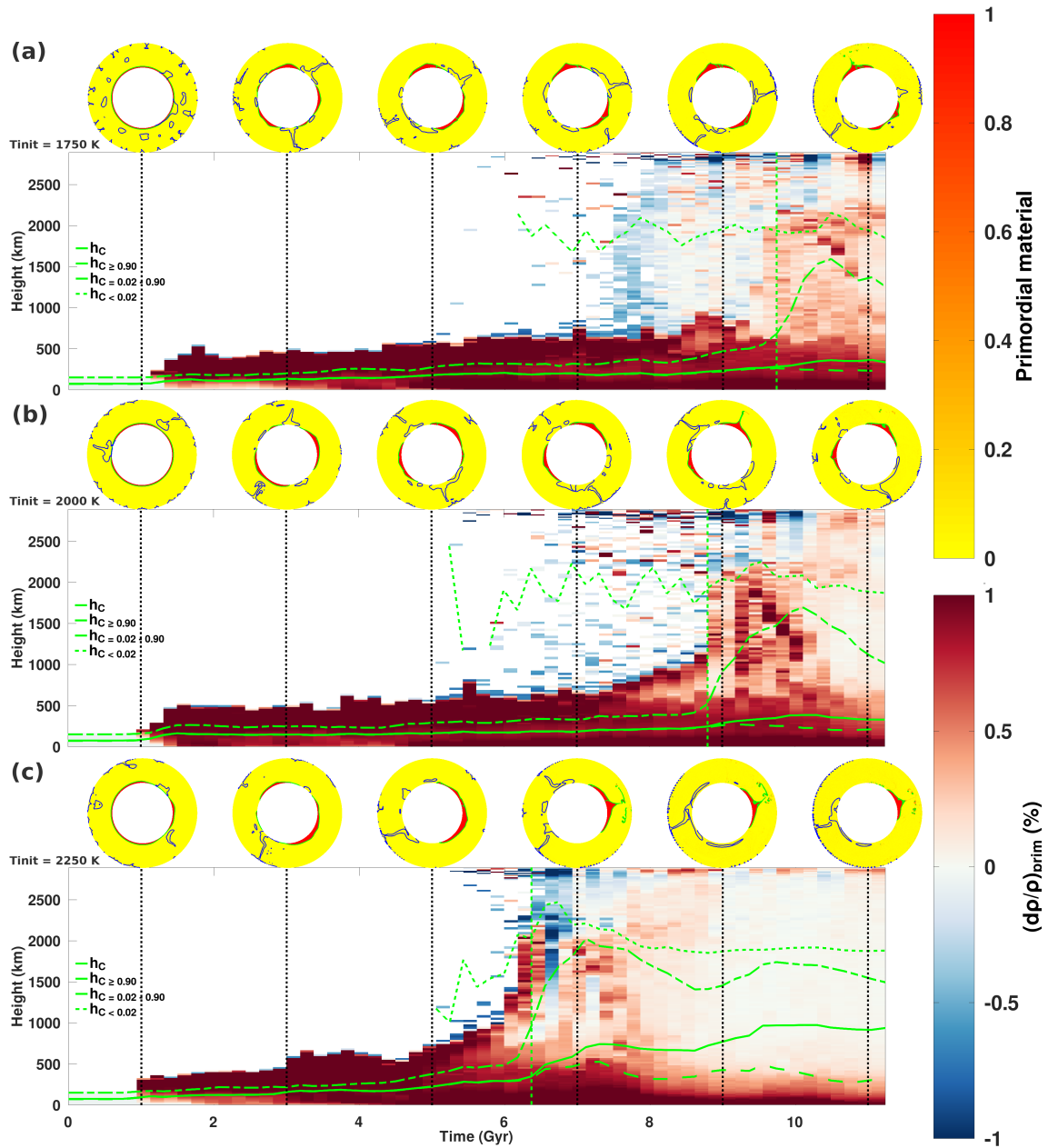
Figure S17. Evolution of the horizontally averaged primordial material density anomalies is illustrated for case no. 17 with increasing initial temperature, T_{init}.

References

Hernlund, J. W., & Tackley, P. J.: Modeling mantle convection in the spherical annulus. Physics of the Earth and Planetary Interiors, 171(1-4), 48-54, https://doi.org/10.1016/j.pepi.2008.07.037, 2008.

Kellogg, L. H., Hager, B. H., & van der Hilst, R. D.: Compositional stratification in the deep mantle. Science, 283(5409), 1881-1884, DOI: 10.1126/science.283.5409.1881, 1999.

Labrosse, S.: Hotspots, mantle plumes and core heat loss. Earth and Planetary Science Letters, 199(1-2), 147-156, https://doi.org/10.1016/S0012-821X(02)00537-X, 2002.

Mosca, I., Cobden, L., Deuss, A., Ritsema, J., & Trampert, J.: Seismic and mineralogical structures of the lower mantle from probabilistic tomography. Journal of Geophysical Research: Solid Earth, 117(B6), https://doi.org/10.1029/2011JB008851, 2012.

Richter, F. M.: Models for the Archean thermal regime. Earth and Planetary Science Letters, 73(2-4), 350-360, https://doi.org/10.1016/0012-821X(85)90083-4, 1985.

Tackley, P. J.: Three-dimensional simulations of mantle convection with a thermo-chemical basal boundary layer: D. The Core-Mantle Boundary Region, Geodyn. Ser, 28, 231-253, https://doi.org/10.1029/GD028p0231, 1998.

Tackley, P. J.: Modelling compressible mantle convection with large viscosity contrasts in a three-dimensional spherical shell using the yin-yang grid. Physics of the Earth and Planetary Interiors, 171(1), 7-18, https://doi.org/10.1016/j.pepi.2008.08.005, 2008.

Tackley, P. J., & King, S. D.: Testing the tracer ratio method for modeling active compositional fields in mantle convection simulations. Geochemistry, Geophysics, Geosystems, 4(4), https://doi.org/10.1029/2001GC000214, 2003.

Trampert, J., Deschamps, F., Resovsky, J., & Yuen, D.: Probabilistic tomography maps chemical heterogeneities throughout the lower mantle. Science, 306(5697), 853-856, DOI: 10.1126/science.1101996, 2004.

Yamazaki, D., & Karato, S. I.: Some mineral physics constraints on the rheology and geothermal structure of Earth's lower mantle. American Mineralogist, 86(4), 385-391, https://doi.org/10.2138/am-2001-0401, 2001.